Chapter 2

Models of molecular line emission from circumstellar disks

Abstract

High-resolution observations of molecular line emission allow the determination of the chemical composition at each radius of protoplanetary disks, providing valuable information (i.e., density, thermal history and composition) about the initial condition of the solar nebula. However, it is impossible to interpret this molecular line emission without knowledge of the transfer of radiation within the object of study. Therefore, we have combined an existing two-dimensional radiative transfer code, *RATRAN* (Hogerheijde & van der Tak, 2000) with a physical disk model based on D'Alessio et al. (2001) and constrained by observations of several CO transitions. In this chapter I will describe this model. In §1, I will provide a discussion of the basic concepts of radiative transfer, including the difficulties in solving the radiative transfer equation and the assumptions that are generally made in order to do so. Non-LTE radiative transfer solutions will be discussed in §2, concentrating on the Monte Carlo method used by *RATRAN*. §3 will describe the physical parameters of our disk model constructed by D'Alessio (private communication) for the T Tauri star LkCa 15, the molecular lines of which have now been studied extensively. The model is used to reproduce the observed CO 2-1 spectrum and the line shape and peak strength of the CO 2-1 transition (Qi et al., 2003) are used to constrain the inner R_{in} and outer R_{out} radius, inclination i, turbulent velocity width Δv, and the scaling factor for the modeled temperature profile. The detailed vertical temperature distribution is also examined through additional fits to observations of the CO 3-2 and CO 6-5 transitions (van Zadelhoff et al., 2001). In §4, these non-LTE models are used to fit the spectra of the 1-0 transitions of ^{13}CO, C^{18}O, HCO$^+$, H^{13}CO$^+$ and N$_2$H$^+$, by scaling the column densities, which are approximated with radial and vertical distributions similar to that of hydrogen. Finally, in §5, the channel maps produced from the resulting models, before and after being sampled at the observed (u, v) coverage, are presented.

2.1 Radiative transfer: Basic concepts

The equation for radiative transfer states that the intensity I of emission at frequency ν integrated along a particular line of sight ds is simply the difference between the flux emitted and absorbed by the dust and gas along the same line of sight, or

$$\frac{dI_\nu}{ds} = j_\nu - I_\nu \alpha_\nu = S_\nu - I_\nu, \tag{2.1}$$

where $\tau_\nu = \alpha_\nu ds$ is the optical depth along the line of sight, α_ν is the absorption coefficent and j_ν is the emission coefficient of the gas and dust combined. (Note: j_ν is the emission coefficient along the line of sight and is related to ϵ_ν the (volume) emission coefficient.) The (line) source function is the ratio of the absorption and emission coefficients, $S_\nu = \frac{j_\nu}{\alpha_\nu}$. For the case when a background source of intensity $\mathrm{I}_\nu(0)$ is included, the solution of the radiative transfer equation (Equation 2.1 above) is

$$I_\nu = I_\nu(0)e^{-\tau_\nu} + \int_0^{\tau_\nu} e^{\tau_\nu - \tau_\nu'} S_\nu d\tau_\nu = I_\nu(0)e^{-\tau_c}[e^{-\tau_\nu} - 1] + S_\nu e^{-\tau_c}[1 - e^{-\tau_\nu}], \tag{2.2}$$

where τ_c is the optical depth in the continuum.

In the absence of collisional excitation, emission and absorption in the gas phase are determined by the rates of spontaneous emission, stimulated emission, and absorption of photons between energy states u and l, with $\Delta\mathrm{E} = \mathrm{E}_u$ - $\mathrm{E}_l = \mathrm{h}\nu_o$. These processes are described by the Einstein coefficients A_{ul}, B_{ul} and B_{lu}, respectively. The emission and absorption coefficients can be written in terms of the Einstein coefficients as

$$\begin{aligned} j_\nu^{ul} &= \frac{h\nu_o}{4\pi} n_u A_{ul} \phi(\nu) && (2.3) \\ \alpha_\nu^{ul} &= n_i \sigma_\nu = \frac{h\nu_o}{4\pi}(n_l B_{lu} - n_u B_{ul})\phi(\nu), && (2.4) \end{aligned}$$

where the 4π comes from an assumption of isotropic emission, σ_ν is the absorption cross section and $\phi(\nu)$ is the normalized line shape, defined such that $\int \phi(\nu)\mathrm{d}\nu = 1$. In the case of Doppler broadening, $\phi(\nu)$ is Gaussian in nature and is given by

$$\phi(\nu) = \frac{c}{b\nu_o\sqrt{\pi}} exp[-\frac{c^2(\nu - \nu_o)^2)}{\nu_o^2 b^2}]. \tag{2.5}$$

It follows that the source function can be defined in terms of the Einstein coefficients:

$$S_\nu = \frac{j_\nu^{ul}}{\alpha_\nu^{ul}} = \frac{n_u A_{ul}\phi(\nu)}{n_l B_{lu} - n_u B_{ul}}. \tag{2.6}$$

Thus, the solution of the equation for radiative transport depends on the level populations through the calculation of the source function. In a two-level system, the level populations are easily calculated from detailed balance, i.e., assuming that the total population of both levels is constant, so that the number of transitions from u to l is the same as from l to u, or

$$n_l(B_{lk}J_\nu + C_{lk}) = n_u A_{kl} + n_u(B_{kl}J_\nu + C_{kl}), \tag{2.7}$$

where the level populations are determined by radiative and collisional processes and C is the collision rate (per second per molecule) of the species of interest. The collision rate depends on the density of the collision partner n_{col} as $C_{ij} = q_{ij}\ n_{col}$ and on the relative velocity of the collision partners (through q_{ij}), with the collision rates for absorption and emission related by

$$C_{lu} = \frac{g_u}{g_l} C_{ul} e^{-\Delta E/kT}. \tag{2.8}$$

Extending this calculation to a multilevel system, the population of one level l depends on the emission and absorption from all other levels $k{\neq}l$ as,

$$n_l[\sum_{k<l} A_{lk} + \sum_{k\neq l}(B_{lk}J_\nu + C_{lk})] = \sum_{k>l} n_k A_{kl} + \sum_{k\neq l}(B_{kl}J_\nu + C_{kl}), \tag{2.9}$$

where the radiation field J_ν is the intensity integrated over all solid angles, $J_\nu = \frac{1}{4\pi}\int I_\nu d\Omega$. The level populations are thus dependent on the radiation field and the source function is in turn dependent on the level populations; the level populations and the intensity I_ν are degenerate. There are several approximations that simplify the problem by decoupling the radiative transfer calculations from the calculation of the level populations. The most common methods involve approximations about the opacity of the gas (in optically thin or optically thick limits), the probability of escape of scattered radiation from the system and the dominance of collisional versus radiative processes, and are summarized briefly next.

2.1.1 Escape probability

If we can replace the source function with a factor that does not depend directly on the level populations or the radiation field, then we can break the degeneracy and solve for J_ν. One such factor is the probability that a photon located at some position in the cloud can escape from the system. For a completely opaque source, the intensity is equal to the source function S. So in terms of the escape probability β, $\mathrm{J} = \int \mathrm{F}_\nu d\nu = S(1-\beta)$. Thus, the level populations become

$$\frac{dn_u}{dt} = n_l C_{lu} - n_u C_{ul} - \beta n_l A_{ul}, \tag{2.10}$$

and are now independent of the radiation field. The escape probability must depend on source geometry and optical depth and therefore has several forms. The most common example is the escape probability for a one-dimensional radially expanding sphere, for which

$$\beta = \frac{1 - e^{-\tau}}{\tau}. \tag{2.11}$$

This is called the Sobolov or large velocity gradient (LVG) approximation. One can define similar escape probabilities for homogeneous slabs, uniform spheres or turbulent media.

2.1.2 LTE and opacity approximations

As shown above, the source function can be written in terms of the Einstein coefficients and level populations as

$$S_\nu = \frac{j_\nu^{ul}}{\alpha_\nu^{ul}} = \frac{A_{ul}}{B_{ul}} \frac{1}{\frac{n_l g_l}{n_u g_u} - 1}. \tag{2.12}$$

The excitation temperature T$_{ex}$ is defined such that

$$\frac{n_u}{n_l} = \frac{g_u}{g_l} exp[\frac{h\nu}{kT_{ex}}]. \tag{2.13}$$

By substituting the definition of the excitation temperature into the equation above we find that the source function is equal to a blackbody radiation field at the excitation temperature T$_{ex}$,

$$S_\nu = \frac{2h\nu^3}{c^2} \frac{1}{e^{h\nu/kT_{ex}} - 1} = B_\nu(T_{ex}). \tag{2.14}$$

In the case of Local Thermal Equilibrium, or LTE, the density becomes sufficiently high (n > n$_{crit}$ = $\frac{A_{ul}}{q_{ul}}$) such that the level populations are controlled by collisional processes, because the timescale for collisions is much less than that of spontaneous emission (C$_{ul}$ $\gg$ A$_{ul}$). The level populations are then solely dependent on the mean free path in the gas, the excitation temperature is equal to the kinetic temperature and the source function (and absorption ceofficient) is now independent of the radiation field, or $S_\nu = B_\nu$ (T$_{kin}$). In this limit, the solution of the equation for radiation transport becomes trivial:

$$I_\nu = B_\nu + e^{-\tau_\nu}(I_\nu(0) - B_\nu). \tag{2.15}$$

If, in addition to LTE, the medium is optically thick, $\tau_\nu \gg 1$, then the intensity approaches that of blackbody radiation ($I_\nu \approx B_\nu$). Similarly, if the medium is optically thin, $\tau_\nu \ll 1$, then the intensity of the emission in a cell is approximately the intensity before passing through the cell, or $I_\nu \approx I_\nu(0)$. This makes the calculation of column densities N$_T$ from observed antenna temperatures (T$_A$) particularly easy by removing the optical depth dependence. For example, for emission in the Rayleigh-Jean limit, the column density of a species is related to the beam-filling factor ($\frac{\Delta\Omega_A}{\Delta\Omega_S}$), where $\Delta\Omega_A$ and $\Delta\Omega_S$ are the solid angles subtended by the antenna (FWHM of the main beam)

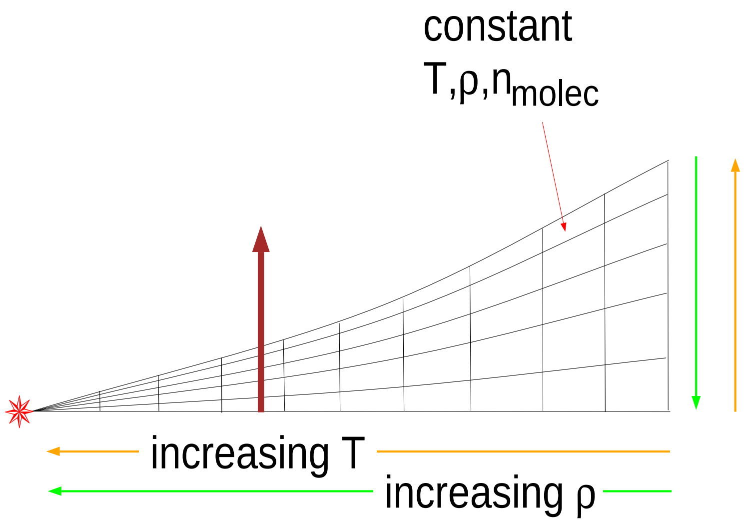

Figure 2.1 This cartoon depicts the grid used for our 2-D Monte Carlo radiative transfer model. Each cell is of constant temperature, total density and density of the molecule in question. Temperature and density variations with radius and height are as indicated. The path of the calculation is indicated by the heavy arrow.

and source, respectively, and the optical depth τ as

$$N_T = \frac{8\pi k\nu^2}{hc^3 A_{ul}} \frac{\Delta\Omega_A}{\Delta\Omega_S} \frac{\tau}{1-e^{-\tau}} T_A \Delta\nu \frac{\sum g_i e^{-E_i/kT}}{g_l e^{-E_l/kT}}, \tag{2.16}$$

where g$_x$ is the degeneracy of level x, $\sum g_i e^{-E_i/kT}$ is the partition function, and T$_A\Delta\nu$ is the equivalent width of the observed line. If we assume that the source fills the beam ($\frac{\Delta\Omega_A}{\Delta\Omega_S} \approx 1$) and if the medium is optically thin ($\frac{\tau}{1-e^{-\tau}} \approx 1$), then

$$N_T = \frac{8\pi k\nu^2}{hc^3 A_{ul}} T_A \Delta\nu \frac{\sum g_i e^{-E_i/kT}}{g_l e^{-E_l/kT}}, \tag{2.17}$$

and the column density can be calculated directly from the observed antenna temperature. In the optically thick limit ($\frac{\tau}{1-e^{-\tau}} \approx \tau$), the column density is easily calculated provided the antenna temperature and the optical depth are known,

$$N_T = \frac{8\pi k\nu^2}{hc^3 A_{ul}} T_A \Delta\nu \frac{\sum g_i e^{-E_i/kT}}{g_l e^{-E_l/kT}} \tau. \tag{2.18}$$

2.2 The non-LTE model

Temperatures indicated by ratios of (sub)millimeter CO emission lines observed toward several protoplanetary disks (van Zadelhoff et al., 2001) indicate that the emission comes from disk surfaces. In these surface layers, the densities are considerably lower than at the disk midplane (see Figures 2.1 and 2.2) and fall short of thermalizing the level populations. Because the conditions are far from LTE the radiation transfer must be calculated explicitly. Additionally, 2-D approaches are necessary to quantitatively treat inclined disks, thanks to the Keplerian velocity fields involved. For this reason we have used an accelerated Monte Carlo model (Hogerheijde & van der Tak, 2000) to solve the two-dimensional radiative transfer and molecular excitation in the LkCa 15 disk, taking both collisional and radiative processes into account. This model produces a simulated observation of each transition as observed by a telescope with resolution equivalent to the model grid for a disk of a given size, inclination and temperature distribution.

The source model is divided into discrete grid cells of constant density, temperature, molecular abundance, turbulent line width, etc. (c.f. Figure 2.1). Thus, the average radiation field (J_ν) is the sum of the emission received in cell i from each of the other cells j after propagation through the intervening cells and weighted by the solid angle subtended by each of these cells j as seen from cell i. The cell size is chosen to be small enough that the molecular excitation is constant throughout the cell. The velocity field is constructed assuming a Keplerian velocity gradient, as expected for circumstellar disks (i.e., Beckwith & Sargent, 1993). The velocity variations within each cell are continuous and integration along a ray is divided into subunits within a cell to track the variation of the velocity projected along the ray.

The radiative transfer code operates by calculating the radiation field J_ν using the equation

$$J_\nu = \Lambda[S_{ul}(J_\nu)], \tag{2.19}$$

where the operator Λ is a matrix that describes how the radiation field of each cell depends on the excitation in all other cells. The source function S_{ul}, which includes the effects of both gas and dust absorption and emission, remains dependent on the level populations; but the model is simplified through iterative solution of equation 2.1 by using the previous level populations and previous S_{ul}. Therefore, J_ν can be evaluated using simple matrix multiplication and the same set of rays can be used throughout the calculation. This method is often referred to as Λ-iteration.

As discussed above, the radiation field of each cell is described by the equation

$$J_\nu = \frac{1}{4\pi}\int I_\nu d\Omega, \tag{2.20}$$

where I_ν is the intensity contribution from all other cells to the radiation field in each of the individual

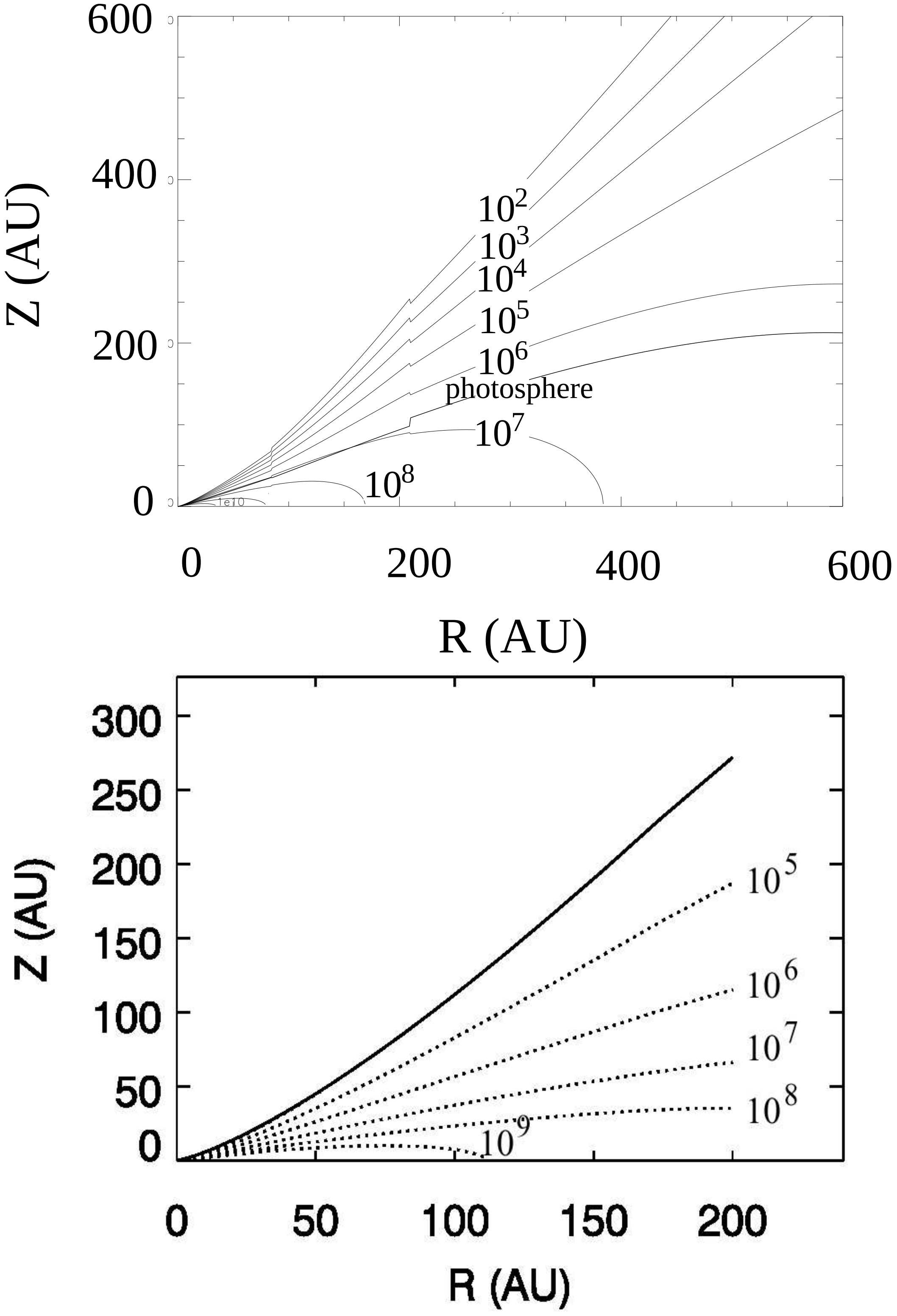

Figure 2.2 Plots of a radial cut of the density distribution for a circumstellar disk as described by the models of (a) Chiang & Goldreich (1997) and (b) D'Alessio et al. (2001).

cells received from the solid angle $d\Omega$. The Hogerheijde & van der Tak model adopts a Monte Carlo approach, approximating this integral by the summation of rays which enter the cell from infinity from a random set of directions and contribute to the radiation field at a random point in the cell's volume. Using this method, the incident radiation is easily separated into local and external radiation fields

$$J_\nu = J_\nu^{external} + J_\nu^{local} = \frac{1}{N}\sum_i I_{0,i} e^{-\tau_i} + \frac{1}{N}\sum_i S_{ul}[1 - e^{-\tau_i}], \tag{2.21}$$

where N is the number of rays i which result in an incident radiation $I_{0,i}$ from a distance to the boundary of the cell ds$_i$. The level populations are used to calculate the source function S_{ul} and the path length ds$_i$ is converted into an opacity $d\tau_i$. In this case the form of the equation used to solve for the radiation field is

$$J_\nu = (\Lambda - \Lambda^*)[S_{ul}^\dagger(J_\nu)] + \Lambda^*[S_{ul}(J_\nu)], \tag{2.22}$$

where Λ^* is the local radiation field and operates on the current source function $S_{ul}^\dagger$. This improves convergence of the calculation for optically thick cells for which the radiation field is close to the local source function.

The approximation of J_ν from a randomly chosen set of directions is valid only if enough directions are included to fully sample the space in sufficient detail. Because the variance σ is dependent on the number of rays N making up J_ν in a particular cell, as $1/\sqrt{N}$, the method arrives at an appropriate sampling by increasing (doubling) N in that cell until the variance drops below a specified value. In this way, each cell has the appropriate sampling; cells close to LTE are not over sampled.

The calculation of J_ν is broken down into two stages. In the first stage, the same set of rays with initially random directions is used to iteratively evaluate J_ν. This iteration is considered complete when the difference between subsequent solutions is a factor of ten smaller than the user-specified level. In the second stage, a different set of rays with random directions is used to calculate J_ν for each iteration. The number of rays is now increased in each iteration (as described above) until the variance drops below a specified value.

The code consists of two parts. The main portion calculates the excitation through the source model, solving the radiative transfer and molecular excitation. The second part of the program integrates the equation of radiative transport,

$$\frac{dI_\nu}{ds} = -\alpha_\nu I_\nu + j_\nu, \tag{2.23}$$

along several lines of sight for a source at a specified inclination angle and distance, calculating the emission that would be observed from this source above the atmosphere and with complete spatial and velocity resolution.

2.3 The physical disk model

The physical disk model, and its effect on the radiative transfer, and in particular the density and temperature gradients, turbulent velocity structure and disk size and inclination, has a large effect on the observed emission. One quadrant of our model is shown schematically in Figure 2.1. With current computers, the three-dimensional codes and sampling needed to examine forming planets are *extremely* slow. Therefore, for simplicity, the disk is approximated as axisymmetric and also symmetric about the disk midplane. Each cell displayed in Figure 2.1 is thus actually a cylinder with its central axis normal to the disk. Stellar radiation is absorbed by dust in disk surface layers and re-emitted in the infrared, warming the disk surface layer and resulting in a flared disk geometry, in which the height of the disk increases with radius from the central star (Chiang & Goldreich, 1997; D'Alessio et al., 2001). As is shown in Figure 2.1, the density increases toward the midplane and toward inner radii. Temperature increases toward the disk surface and, of course, toward radii closer to the star.

As mentioned above, stellar radiation and its absorption, scattering and reradiation by dust has a large effect on the temperature gradient through heating of disk surface layers, which in turn affects the degree of flaring of the disk and thus the portion of the disk in the direct line of sight of stellar radiation. There are several models that simulate the effect of the reprocessing of stellar radiation. In this work, we model the radiation transfer for disks using the temperature and pressure gradients calculated by D'Alessio et al. (2001), who calculate disk structure self-consistently assuming complete mixing and thermal balance of the gas and dust. The pressure as a function of height is determined by calculations of vertical hydrostatic equilibrium. The temperature gradients and variation of the pressure as a function of radius are controlled by energy produced via viscous dissipation, radioactive decay (primarily of ^{26}Al), cosmic rays and stellar irradiation and transport of this energy by turbulent flux (radially and vertically), radiation and convection.

In the D'Alessio model, the solid phase is composed of silicates (olivine and orthopyroxene, see Chapter 5), water ice, troilite and organics in mass fractional abundances of 4.4:1:7.3:5.4. The grains have a powerlaw size distribution $n(a) = n_o\ a^{-p}$, where a is the grain radius, n_o is a normalization constant and the exponent p is a free parameter. The input parameters for the LkCa 15 model were taken from the literature, with a uniform disk mass accretion rate of $\dot{M} = 1.0\times10^{-8}$ M$_\odot$/yr, stellar mass M$_* = 1$ M$_\odot$, stellar radius R$_* = 1.64$ R$_\odot$, and stellar temperature T$_* = 4395$ K. The turbulent viscosity is described by the parameter $\alpha = 0.01$–0.001, which was fit to the disk mass (0.01 is consistent with the Balbus-Hawley magnetohydrodynamical instability; Hawley & Balbus, 1991). The maximum grain size was found to be a$_{max} = 1$ mm with the powerlaw exponent of the size distribution $p = 3.5$. This maximum grain size indicates that silicates dominate the SED at $\lambda = 1$ mm, troilite dominates in the cm range, and in the mid- and far-IR, water ice and organics

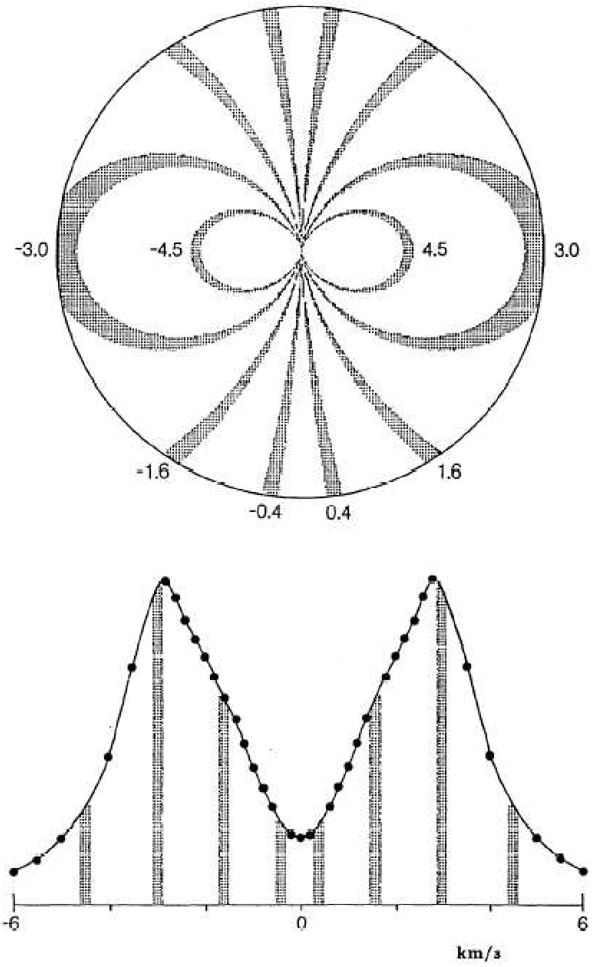

Figure 2.3 Translation of disk position and velocity for an inclined disk, taken from Beckwith & Sargent (1993). The shaded regions in the diagram of the disk (top) correspond to the velocities in the spectrum (bottom) via the equation $r(\phi) = \frac{GM}{v_{obs}^2} \sin^2\theta \cos^2\theta$.

dominate the SED. This is consistent with the SED for LkCa 15 (Chiang et al., 2001). Mie scattering (Wiscombe & Joseph, 1977) is used to calculate the absorption efficiency (Q_{abs}), treating the grains as spheres for simplicity.

A disk of material rotating in Keplerian motion ($v_{Kep} = (\frac{GM}{R})^{1/2}$) about a central star which is inclined with respect to the observer exhibits a double peaked spectrum as the line of sight encounters material moving with different orbital velocities. The emission line profile can be thought of as a sum of the independent emission from each position in the disk, modified by the appropriate Doppler shift due its radial motion ($v_D = v_{Kep}$ sin$i$ sinθ), characterized by the azimuthal angle θ and the inclination angle i between a vector normal to the disk plane and the observer's line of sight. For the case of an inclined disk, the translation between disk position $r(\phi)$ and projected velocity v_{obs}

(Figure 2.3; Beckwith & Sargent, 1993) is

$$r(\theta) = \frac{GM}{v_{obs}^2}\ \sin^2 i\ \cos^2\theta. \qquad (2.24)$$

The line shape, in particular the separation and sharpness of the peaks, is indicative of the disk inclination, size, temperature and turbulent velocity width as well as the column density of the emitting material (c.f. Horne & Marsh, 1986; Beckwith & Sargent, 1993), for

$$F_\nu(v_{obs}) = \frac{4}{4-q}\ \frac{2kT_d\nu^2}{c^2}\ \frac{R_{out}^2}{D^2}\ \frac{\Delta v_d}{v_d}\ (\frac{v_{obs}}{v_d})^m, \qquad (2.25)$$

where $v_d = (GM/R_{out})^{1/2}$ is the velocity at the outer edge of the disk R_{out}, q is the powerlaw index of the temperature distribution ($T(r) = T_d(\frac{r}{R_d})^{-q}$), D is the distance to the disk from the observer, and $\Delta v_d = (2kT_d/m_0)^{1/2}$ is the local velocity dispersion. The value of m varies from $m = 3q - 5$ in the high-velocity limit to $m = 1$ in the low velocity limit, indicating a double peaked profile, with peak values occurring at $v_{obs} = \pm v_d$ and a decreasing flux toward low velocities.

We can use the observed CO emission and the relationships described above to constrain the physical structure of disks. Figure 2.4 shows how the modeled CO 2-1 emission spectrum for LkCa 15 changes as the disk parameters are varied. The scale factor for the disk temperature and the inclination, turbulent velocity width ($\delta v^2 = \frac{2kT}{m_0} + v_{turb}^2$) and disk limits R$_{in}$ and R$_{out}$ were selected to best match the observed CO 2-1 emission. As the disk temperature T_d is increased (keeping the distribution of temperature with radius constant), the total flux of the emission line and the strength of the peaks relative to the flux at the line center also increase. Because the CO 2-1 emission line is optically thick, the disk temperature is very similar to the gas brightness temperature. Increasing the outer radius of the disk [1]results in an increase in the flux of the line emission, but little change in the line shape. The line center flux depends is proportional to R$_{out}^2$ and increasing R$_{out}$ fills in the region between the two peaks. We find that an outer radius of R$_{out}$=426 AU is necessary to fit the CO 2-1 emission, which is consistent with that required from fits to the integrated intensity maps with a 2-D Gaussian (Qi et al., 2003). An inner radius cutoff of R$_{in}$ $\leq$ 5 AU is required to fully sample the inner disk radii and replicate the image of CO 2-1 in LkCa 15. The double peaked nature of the line shape arises from material rotating at an angle inclined to the line of sight and thus is strongly affected by the disk inclination (as $\sin^2 i$), with emission from a face on orientation being single peaked. The double peak widens with increased inclination from face on (see Horne & Marsh, 1986) and an inclination of 60° with the disk surface facing toward the observer best matches the spectrum and gives minimal residuals when compared to the integrated intensity map of CO 2-1 toward LkCa 15. This is consistent with the intensity obtained via fitting the integrated intensity

---

[1] The D'Alessio model has a maximum outer radius of R$_{out}$ = 500 AU. In order to explore the extension of the outer radius beyond 500 AU, we expand the model to farther radii by keeping the disk parameters (i.e., hydrogen density, temperature, pressure) constant at the same values as the outermost cell of the D'Alessio model.

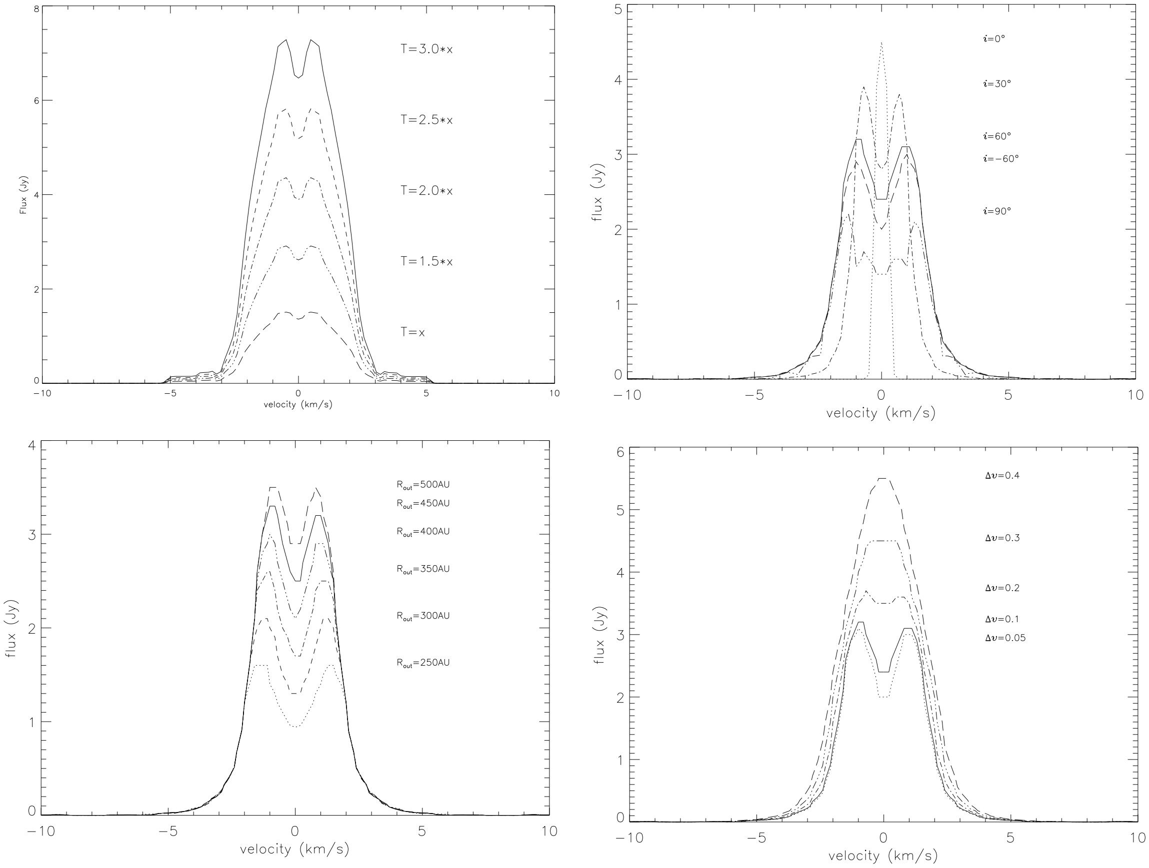

Figure 2.4 This figure indicates the response of the model for the CO 2-1 transition to variations in the physical parameters of the disk. (a) The emission line strengthens and sharpens as the temperature is increased through scaling of the profile from D'Alessio et al. (2001), denoted by x. (b) The peak shape changes drastically from a narrow single peak when the disk is oriented face on ($i = 0°$) to a broad double peak when the disk is edge on ($i = 90°$). (c) Increasing the outer radius R_{out} results in increased line strength and a decrease in the separation between the peaks, because the emission near the line center arises from the outer disk. (d) Increasing the turbulent velocity width (Δv) essentially increases the interaction between material in different radii, thus smearing the emission line; with $\Delta v = 0.05$ km/s the line shape is virtually unchanged and for $\Delta v = 0.4$ the double peak completely disappears.

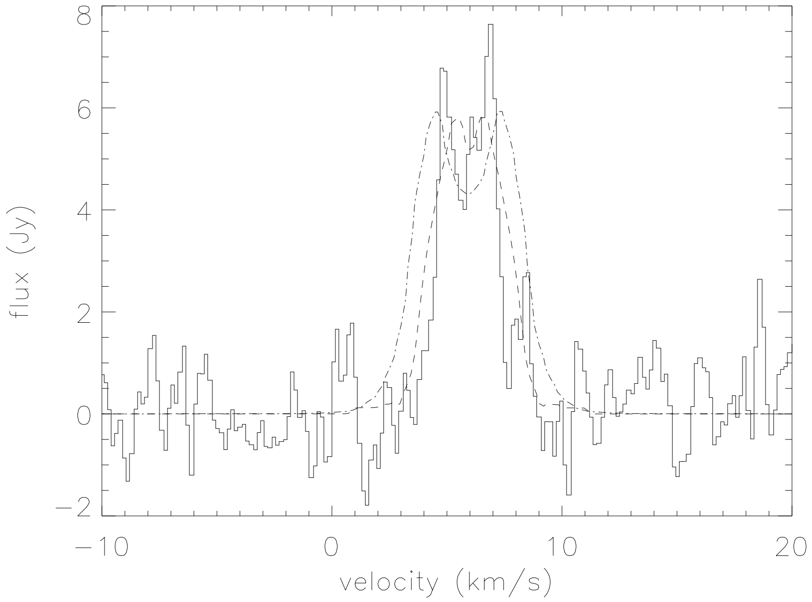

Figure 2.5 CO is a good tracer of disk structure and kinematics. Here we use our model to show that CO emission from the LkCa 15 disk (solid line) is well matched to model CO emission (dotted/dashed lines) from a disk with an inclination of 58 degrees, a turbulent velocity of 0.1 km/s and an outer radius of 430 AU. This model assumes that the CO abundance can be simply scaled from the hydrogen abundance, which appears to be sufficient for this optically thick emission. The dotted and dashed lines are models using temperature distributions as calculated by Chiang & Goldreich (1997) and D'Alessio et al. (2001). The simple two-layer model of Chiang & Goldreich (1997) produces temperatures that are too high to fit our data.

maps assuming that the disk is circular. Variation in the turbulent broadening width also has a large effect on the line shape. A turbulent velocity width of less than 0.2 km/s is necessary for the spectrum to be double peaked and a turbulent velocity width of $\Delta v = 0.1$ km/s best fits the splitting of the observed double peaked spectrum (see Figures 2.4 and 2.5). In summary, the best agreement with the observed spectrum and map of CO 2-1 emission toward LkCa 15 is a disk with an inner radius and outer radius cutoffs $R_{in} = 5$ AU and $R_{out} = 426$ AU inclined toward the observer with $i = 60°$ and a turbulent velocity width $\Delta v = 0.1$ km/s. In these simulations, the column density of CO is scaled from the D'Alessio et al. (2001) hydrogen density as 10^{-5} N_H.

Observations of high-J transitions can provide additional information about the temperature structure in the disk. For this reason, observations of CO 3-2 and CO 6-5 emission from LkCa 15 were obtained at the Caltech Submillimeter Observatory (van Zadelhoff et al., 2001). Using the model described above, with all other parameters held constant, the temperature scale factor was varied until the CO 3-2 and 6-5 spectra were fit. The resulting temperatures as a function of radius are shown in Figure 2.6. The temperature increases with increase in J, indicating that the high-J levels probe material closer to the disk surface. In essence what we have obtained is the temperature

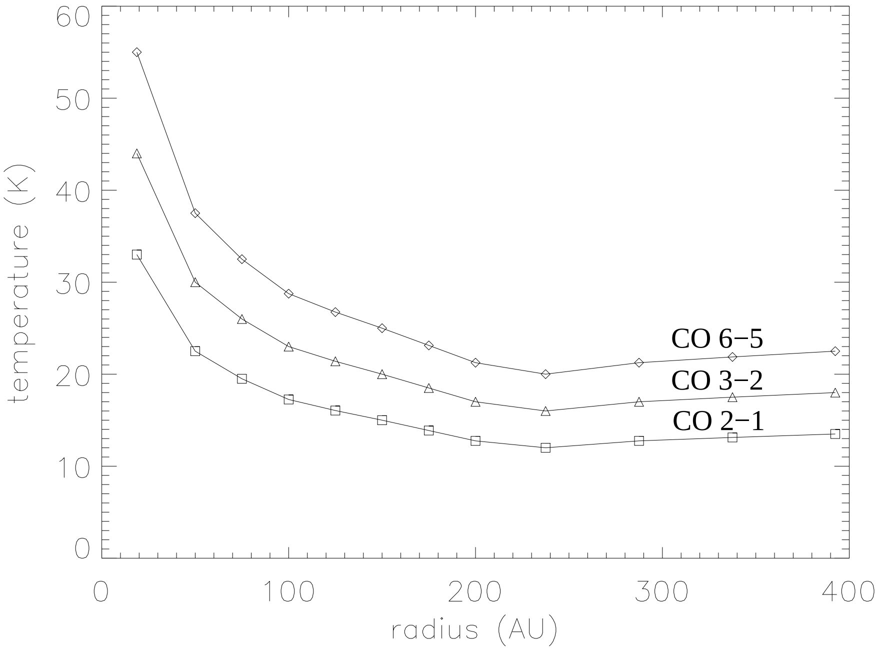

Figure 2.6 Temperature distributions required to fit the observed CO 2-1, 3-2, and 6-5 transitions toward LkCa 15. The temperature increases for transitions with increasing J, indicating that these high-J transitions probe warmer gas, at higher vertical heights within the disk.

as a function of height in the disk; the temperature ranges from 30–60 K on the disk surface near the star, but temperatures are much cooler 15–30 K in the outer regions of disks ($R > 75$ AU) to which we are sensitive with OVRO. This temperature structure is very similar to that predicted with the D'Alessio et al. (2001) and Chiang & Goldreich (1997) models.

2.4 Comparing models with observations: Constant column density calculations

We have used the non-LTE accelerated Monte Carlo model described above (Hogerheijde & van der Tak, 2000), with the disk parameters now fixed, to solve the two-dimensional radiative transfer and molecular excitation for several other molecular transitions observed with OVRO toward the LkCa 15 disk. This model produces a simulated image of each transition as observed by a telescope with a resolution equivalent to the model for a disk of a given size, inclination and temperature distribution. The MIRIAD function UVMODEL and the observed visibility data set were used to sample this model at the observed (u, v) spacings and the model data set was processed in a manner identical to that of the OVRO data, thus allowing a direct comparison of the two. For each transition observed, the integrated line intensity was calculated from the resulting model and compared to the

Table 2.1. Observed molecular intensities and column densities toward LkCa 15

Transition	Beam (arcsec)	$\int T_A dv$(LTE) (K km/s)	N(30K,LTE) (cm^{-2})	N(Model) (cm^{-2})	Model Ratios N(Model)/N(30K,LTE)
CO 2-1	1.81×1.49	12.5	7.28(15)	1.68(18)	230
^{13}CO 1-0	2.74×2.41	6.39	1.11(16)	3.04(16)	2.74
C^{18}O 1-0	5.05×3.59	1.90	3.31(15)	1.40(15)	0.42
HCO$^+$ 1-0	7.74×5.64	3.30	9.25(12)	2.31(13)	1.79
H^{13}CO$^+$ 1-0	6.30×4.41	<0.88	<2.60(12)	<1.12(12)	0.43
N$_2$H$^+$ 1-0	3.51×3.17	3.83	1.71(13)	3.07(13)	1.80

observed integrated line intensity. Iteration of the model over a range of column densities for each observed transition was performed to provide a fit to the observed integrated line intensity. The column density was assumed to be constant as a function of radius. This is consistent with the results of various chemical models (Willacy & Langer, 2000; Aikawa & Herbst, 1999) at the large radii ($>$ 50 AU) to which we are sensitive with the current OVRO Millimeter Array. For these model calculations, the temperature and hydrogen density as a function of radius and height were acquired from the model of D'Alessio et al. (2001), calculated specifically for the stellar parameters of LkCa 15.

The resulting column densities are shown in Table 2.1. The column densities calculated using this non-LTE radiative transfer model are 1–2 orders of magnitude larger than those calculated in the Willacy & Langer (2000) models of disk chemistry, but consistent with those calculated by Aikawa & Herbst (2001). As indicated in the last column of Table 2.1, for CO 2-1, ^{13}CO 1-0, HCO$^+$ 1-0 and N$_2$H$^+$ 1-0 emission the column densities are smaller when calculated using the LTE assumption. This is due to the fact that the emission from these transitions is optically thick. The LTE calculations assume that the gas is optically thin and that the entire disk is being probed by the line emission and thus result in an underestimation of the total amount of CO, HCO$^+$ and N$_2$H$^+$ present. Comparison of the CO isotopologues and HCO$^+$ and H^{13}CO$^+$ agree with the assessment that the CO 2-1, ^{13}CO 1-0 and HCO$^+$ 1-0 transitions are optically thick (see above discussion). In the case of the C^{18}O 1-0 and H^{13}CO$^+$ 1-0 emission, which are believed to be optically thin, the column densities are overestimated when thermal equilibrium is assumed. This supports the conclusion that conditions in the emitting region are not at LTE, and that both radiative and collisional processes play a part in the excitation. The population of higher energy rotational states is thus much lower than would be the case if collisions were dominant; and the assumption of thermal equilibrium therefore results in an overestimation of the population of the upper states and thus in the total column density, which at LTE is directly proportional to the density of the upper state.

A curve of growth, or plot of the equivalent width (W_λ) of the line (or line flux) and the number

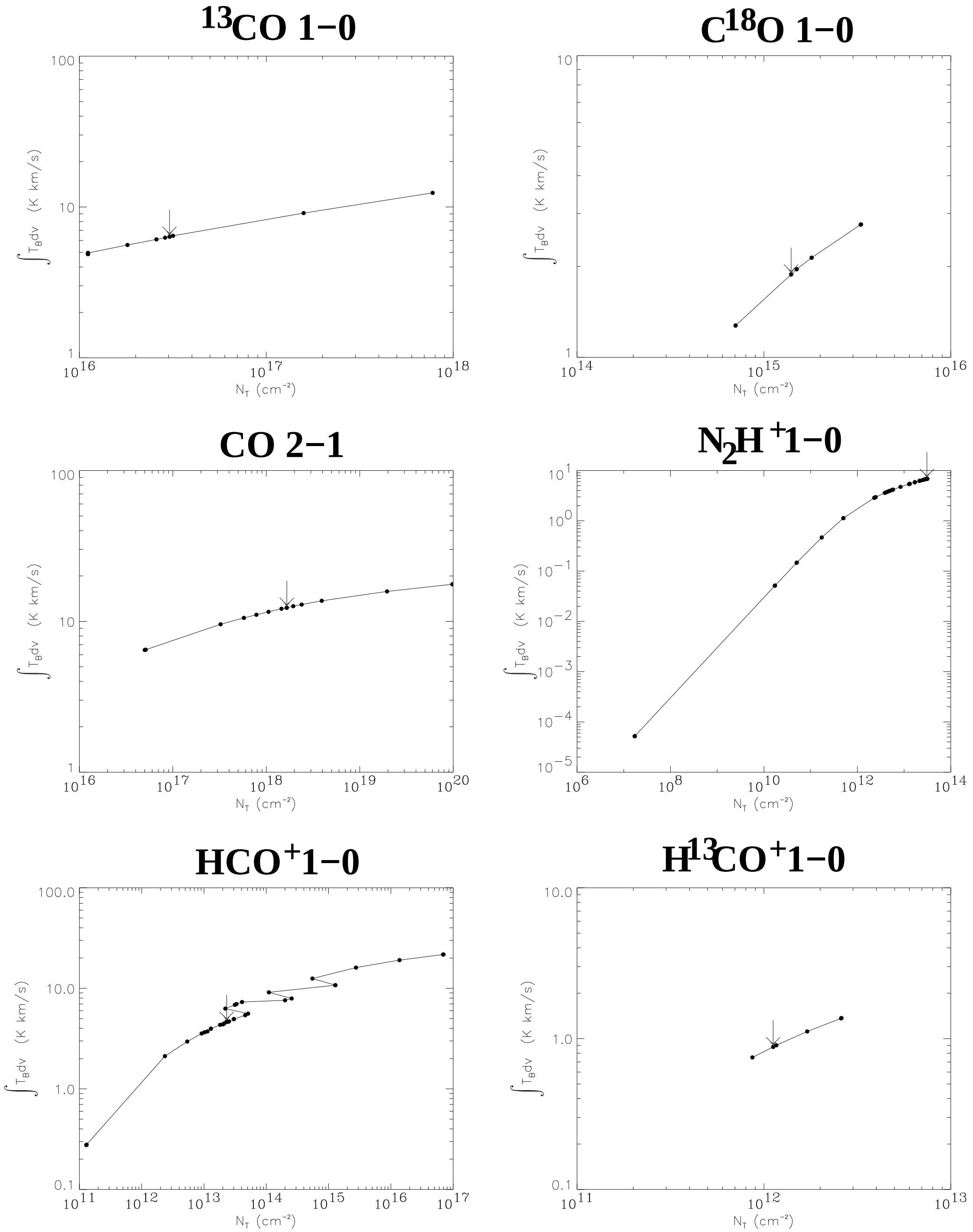

Figure 2.7 Curve of growth analysis for the constant column density model. The arrows depict the points where a successful fit to the observed spectrum was obtained. For the optically thick transitions, ^{13}CO 1-0, CO 2-1, HCO$^+$ 1-0 and N$_2$H$^+$ 1-0, the column densities are approaching the flat part of the curve of growth and therefore the integrated intensity is not extremely sensitive to column density. C^{18}O 1-0 and H^{13}CO$^+$ 1-0 appear to be optically thin, with the integrated intensity linearly related to the column density.

of absorbers ($N_j f_{jk}$, where N_j is the column density and f_{jk} is the oscillator strength), is often used to describe the sensitivity of an observation to changes in the (column) density of a molecule. In order to evaluate how sensitive our models are to changes in the column density of the observed species, we performed a slight variation on the standard curve-of-growth analysis. In this analysis, we plot the integrated intensity ($\int T_B dv$) of the modeled line is versus the column density N_T as shown in Figure 2.7 for the transitions discussed above. We find that for ^{13}CO 1-0, CO 2-1, HCO$^+$ 1-0 and N_2H^+ 1-0 the column densities are approaching the flat part of the curve of growth and therefore the integrated intensity is not extremely sensitive to column density. However, for C^{18}O 1-0 and H^{13}CO$^+$ 1-0 the relationship appears to be closer to the linear part of the curve of growth. The curve of growth is linear when the total rate of energy emission varies linearly with the number of molecules, meaning that emission from essentially each molecule reaches the observer. Thus, the curve of growth is directly related to the optical depth, and C^{18}O 1-0 and H^{13}CO$^+$ 1-0 are in the linear region of the curve of growth because these transitions are optically thin. In this manner, our model is also sensitive to optical depth, with the most accurate estimates of the column densities coming from the analysis of optically thin transitions.

2.5 Comparing models with observations: Imaging

Molecular distributions are essential to understanding the chemistry taking place in disks. However, proper interpretation of interferometric observations require an understanding of the effects of telescope resolution and incomplete sampling of the (u, v) plane. For this reason, we use our model to simulate images of the observed CO 2-1 emission toward LkCa 15, in two scenarios: 1) the observations were made using an array with complete UV coverage that matches the model resolution, and 2) the observations were made under the same conditions as the OVRO observations. Comparison of these two will help us understand what information is lost due to the imperfections of real observations. In both cases, the models are produced with the parameters (R_{out}, i, Δv, etc.) derived above for the CO 2-1 emission toward LkCa 15. The first scenario is the default output from the $RATRAN$ radiative transfer code (Hogerheijde & van der Tak, 2000). To simulate the observations, the models are resampled at the observed (u, v) coverage and resolution by replacing the amplitudes of the observed visibilities with the model amplitudes at the same positions.

It is easiest to see the differences between these two scenarios in channel maps displaying the integrated intensity in 0.6 km/s channels, which demonstrate how the material of different velocities is distributed (Figure 2.8). These channel maps are equivalent to taking the shaded regions of Figure 2.3 and plotting each on its own map. The top panels show the perfect telescope scenario. These channel maps are very similar to what we would expect from Figure 2.3. The "butterfly" shape of the observed emission in each channel arises from the distribution of material with the same

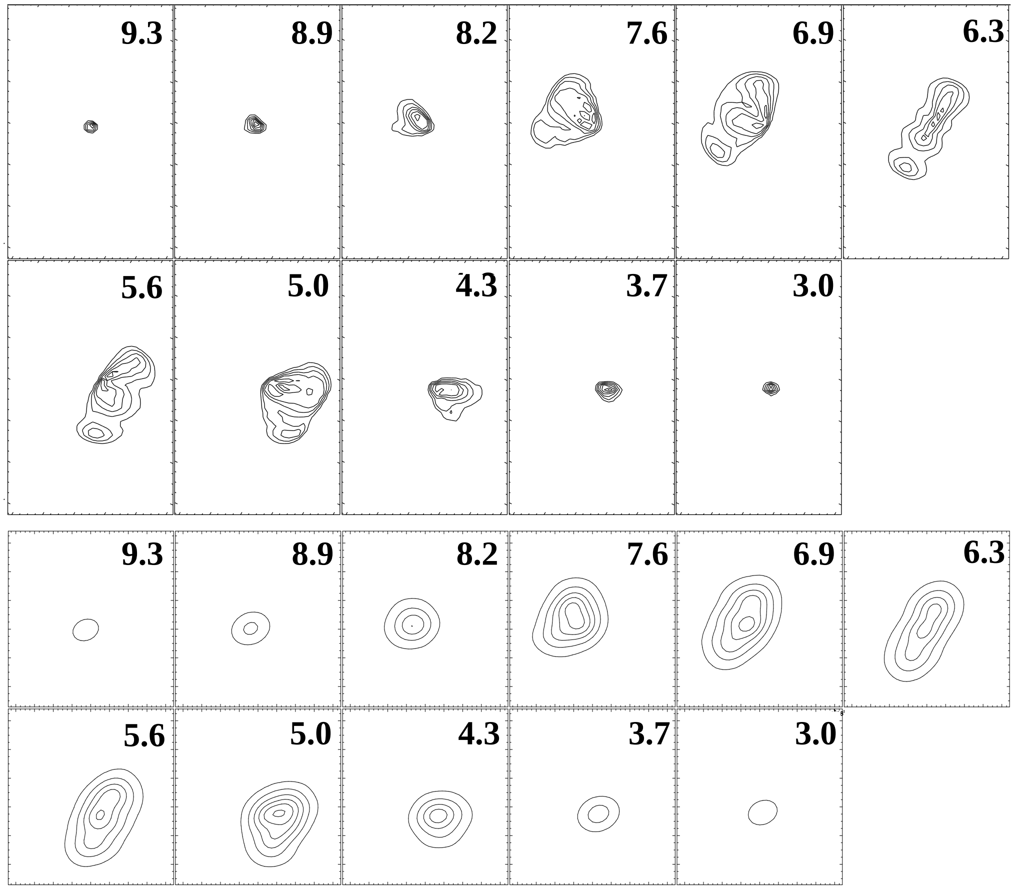

Figure 2.8 Channel maps produced using the model described above to simulate observations of CO 2-1 emission from LkCa 15. The unconvolved channel maps (top) are equivalent to observations using an array with complete sampling of the (u, v) plane to a resolution that matches that of the model. These maps depict a migration from left to right as the velocity shifts from red to blue around the systemic (average) velocity (∼6.3 km/s). The channel maps on the bottom result from sampling the original model at the observed (u, v) coverage (θ_{beam} ∼2″). This has the effect of smoothing out the structure seen in the previous maps, and making the shift in position with velocity less evident. The difference between these models indicate the importance of (u, v) coverage to the interpretation of such observations.

velocity in the disk. In the case of our simulation, emission from material with velocities to the red (blue) of the line center, shows up to the west (east) of the stellar position. From the spectrum of CO 2-1 toward LkCa 15 (Figure 2.5), the line center is at ~6.3 km/s with a velocity range of about ±3 km/s, consistent with these channel maps. The small peak toward the south is due to the fact that the disk has a finite radius and is flared; when inclined at 58°, a corner of the underside of the disk is visible and this is the peak that we see. The bottom panels show the resulting channel maps when the model is sampled at the observed (u, v) coverage and resolution ($\sim 2''$). This has the effect of smoothing out the structure seen in the previous maps, and making the shift in position with velocity less evident. It is quite astonishing how big the change is between these scenarios. The difference between these models indicates the importance of (u, v) coverage to the interpretation of such observations. This is particularly important when analyzing more complicated molecular distributions as discussed in Chapters 3 and 4.

2.6 Summary

A non-LTE Monte Carlo radiative transfer model (Hogerheijde & van der Tak, 2000) was used to simulate molecular line emission from the T Tauri star LkCa 15 disk. Temperature distributions and hydrogen densities from D'Alessio (private communication) calculated for a star with $M_* = 1\ M_\odot$, $R_* = 1.64\ R_\odot$, $M_* = 4395$ K, $\dot{M} = 1.0\times10^{-8}\ M_\odot$/yr were used. Fits to the CO 2-1 emission establish the physical parameters of the model; the best agreement with the observed spectrum and map is a disk with inner radius and outer radius cutoffs $R_{in} = 5$ AU and $R_{out} = 426$ AU inclined toward the observer with $\imath = 60°$ and a turbulent velocity width of $\Delta v = 0.1$ km/s. These models were used to solve the radiative transfer and molecular excitation for the observed 1-0 transitions of ^{13}CO, C^{18}O, HCO$^+$, H^{13}CO$^+$ and N$_2$H$^+$ using the physical model described above and varying the fractional abundance of each molecule to match the integrated intensity. The resulting column densities are larger by a factor of ~2 than those predicted from a standard LTE, $\tau \ll 1$ analyses for ^{13}CO, HCO$^+$, and N$_2$H$^+$, which are believed to be optically thick, and smaller than those predicted from a standard LTE, $\tau \ll 1$ analyses for C^{18}O and H^{13}CO$^+$, which are optically thin. This indicates that the emitting regions are not at LTE and that optical depth effects play a large role in the relationship between column densities and observed integrated intensities in the regions probed by low-J transitions of molecular gas in circumstellar disks. The models were also used to simulate integrated intensity and channel maps of the emission for a telescope with essentially infinite resolution and complete (u, v) coverage and for the observed (u, v) spacings for CO 2-1. Even with $2''$ resolution it was found that detailed disk structure is largely undersampled by current observations and image deconvolution techniques.

Bibliography

Aikawa, Y. & Herbst, E. 1999, ApJ, 526, 314

—. 2001, A&A, 371, 1107

Beckwith, S. V. W. & Sargent, A. I. 1993, ApJ, 402, 280

Chiang, E. I. & Goldreich, P. 1997, ApJ, 490, 368

Chiang, E. I., Joung, M. K., Creech-Eakman, M. J., Qi, C., Kessler, J. E., Blake, G. A., & van Dishoeck, E. F. 2001, ApJ, 547, 1077

D'Alessio, P., Calvet, N., & Hartmann, L. 2001, ApJ, 553, 321

Hawley, J. F. & Balbus, S. A. 1991, ApJ, 376, 223

Hogerheijde, M. R. & van der Tak, F. F. S. 2000, A&A, 362, 697

Horne, K. & Marsh, T. R. 1986, MNRAS, 218, 761

Qi, C., Kessler, J. E., Koerner, D. W., Sargent, A. I., & Blake, G. A. 2003, ArXiv Astrophysics e-prints

van Zadelhoff, G.-J., van Dishoeck, E. F., Thi, W.-F., & Blake, G. A. 2001, A&A, 377, 566

Willacy, K. & Langer, W. D. 2000, ApJ, 544, 903

Wiscombe, W. J. & Joseph, J. H. 1977, Icarus, 32, 362